Cement & Concrete Composites 33 (2011) 457–465

Contents lists available at ScienceDirect

Cement & Concrete Composites

journal homepage: www.elsevier.com/locate/cemconcomp

Validity of recent approaches for statistical nanoindentation of cement pastes

Pietro Lura *, Pavel Trtik, Beat Münch

Empa, Swiss Federal Laboratories for Materials Science and Technology, Switzerland

ARTICLE INFO

Article history:
Received 8 June 2010
Received in revised form 17 January 2011
Accepted 18 January 2011
Available online 25 January 2011

Keywords:
Statistical nanoindentation
Focussed-ion beam nanotomography
Cement paste
Microstructure

ABSTRACT

In this paper we proceed in the examination of different aspects of the application of statistical nanoindentation to hydrated cement pastes for determining the mechanical properties of the single phases. In particular, we evaluate the size of the uniform domains of hydration products in a volume of cement paste obtained by Focussed-Ion Beam Nanotomography and we show that the uniform domains are too small to origin separate peaks in the frequency plots. Finally, we show that the procedure of fitting the frequency plots by Gaussian distributions of different sizes is not robust and heavily relies on assumptions about the elastic properties of the different phases.

1. Microstructure and statistical nanoindentation

In statistical indentation performed on a multiphase material, a large number of single indentation tests are performed in a grid, without any knowledge of the microstructure at the position of indentation [1]. The indentation elastic modulus histograms are then analyzed with statistical methods, in order to extract the mechanical properties of the single phases [1]. According to Constantinides and Ulm [1], the interaction volume for nanoindentation in cement paste is in the range of $v = 1\ \mu m^3$, or larger.

In a recently published paper [2], we argued that statistical nanoindentation at the currently used nanoindenter size [3,4] cannot be applied for determining material properties of single phases in hardened cement paste, mainly due to their fairly complex micro- and nanostructure.

In our paper [2], we first presented virtual experiments emulating statistical nanoindentation on 3D images of an idealized two-phase material composed of gray and black cubes of side D (3D checkerboard), to which different elastic moduli values were assigned. We never meant with this simulation to compare the highly complex microstructure of cement pastes with such elementary patterns (compare with Ulm et al. [3]). The 3D checkerboard virtual experiment proved instead that the potential of statistical nanoindentation is limited even on extremely simplistic structures. Since statistical nanoindentation fails even on simple microstructures, its applicability to the highly complex microstructure of cement pastes needs to be questioned (see Section 2 in this paper).

A further step was reproducing a virtual statistical indentation experiment based on a Focussed-Ion Beam Nanotomography (FIB-nt) dataset of a hardened cement paste with water to cement ratio 0.3 [2]. Elastic modulus histograms with multiple peaks were obtained even in the case of a material that was segmented into three phases only (porosity, hydrated and unhydrated phases), i.e., without the hydrated phase being composed of different types of hydration products [2]. Hence, peaks that are identified in the literature as belonging to LD and HD C–S–H could in reality equally reflect the presence of only one type of C–S–H next to other crystalline phases of high elastic moduli (e.g., unhydrated cement, calcium hydroxide, ettringite) within the indentation interaction volume [2].

It is interesting to compare our conclusions with a recent paper [5]. Chen et al. [5] examined a low water/cement ratio (w/c 0.20) hydrated Portland cement paste by statistical nanoindentation coupled with ex situ scanning electron microscope-energy-dispersive X-ray spectra (SEM–EDS) analysis at each indentation point. As the volumes probed by each method were considered to be of similar size (~2 μm), the mechanical information provided by nanoindentation was directly comparable to the chemical information provided by SEM–EDS. In Fig. 4 of [5], probability density distributions of indentation modulus and indentation hardness are shown. The distributions are decomposed by phases, i.e., clinker, inner product/interface between phases, outer product, and pores/defects. Remarkably, points corresponding to clinker were found from 160 GPa down to a modulus of 30 GPa. All the peaks found in the probability distribution appear to correspond to mixtures of two or more phases. We believe that these new results [5] support our critique of the statistical nanoindentation method as we formulated it in [2]. Moreover, we consider the approach of Chen et al. [5], of combining indentation with microstructural

* Corresponding author.
E-mail address: pietro.lura@empa.ch (P. Lura).

0958-9465/$ - see front matter © 2011 Elsevier Ltd. All rights reserved.
doi:10.1016/j.cemconcomp.2011.01.006

investigations (whether SEM–EDS [5,6] or FIB sectioning [2,7,8]) as a promising way to study the local mechanical properties of cement paste and of its constituents.

Continuing in the line of thought presented in [2], in this paper we proceed further in the examination of the fundamentals of statistical nanoindentation applied to hydrated cement pastes. In particular in Section 2, we investigate the relationship between the size of the uniform domains of hydration products in image data from cement paste and the statistical nanoindentation results. Finally in Section 3, we question the robustness of the fitting procedure of the frequency plots by Gaussian distributions of different sizes.

2. Geometric structure of areas with uniform phases and usability of the phase distribution

A possible point of criticism to our foregoing study [2] might be the chosen method for estimating the local elastic moduli from the 3D volumetric mask [3]. We agree that this is a key element in the chain of evidence questioning nanoindentation experiments on cement pastes presented in [2]. In the following investigations, this controvertible point is therefore completely omitted. All results presented in this section are based on the phase geometry only, which was achieved by means of high-resolution FIB-nt.

Let us suppose a system with a limited number of phases with known 3D structure. The following virtual nanoindentation experiment requires two assumptions:

Assumption 1. Let v be the interaction volume probed by a nanoindenter in a cement paste, assumed equal to 1 μm^3 [1].

Assumption 2. Take a 3D data volume acquired with the help of a FIB-nt system [9,10] and assume that the geometry of the phases which can be extracted and segmented provides some realistic reflection about the structure of the actual phases. In fact, the effective phase structure is much more complicated, since there are by far more phases available than only the three (i.e., pores, hydration products and unhydrated cement) that can be clearly distinguished and segmented [11]. Hence, the extracted structure can be postulated to represent a lower bound of the real microstructural complexity in a cement paste.

According to assumptions 1 and 2, segmented 3D FIB-nt volumes are used as model phase structures for significance studies of nanoindentation experiments on cement paste.

Consequence. From assumptions 1 and 2, it follows directly that, for raising any statement about the true phase distribution of a material structure by means of statistical nanoindentation, the phase distributions of the examined interaction volumes need phase composition values leading to distinguishable clusters at each phase. This condition cannot be accomplished if v is too large. In other words, if a composite is probed by statistical indentation with size of the interaction volume v, the resulting set of the phase compositions of the interaction volumes must exhibit unequivocal peaks at each original phase. For the present experiment with foreknown phase geometry, this means that peaks around the known phases ultimately must occur in a phase diagram. If this condition is not met, the cause can be one of two: either the measured phase geometry is different from the native structure of the observed cement paste, or the nanoindentation interaction volume is too large for probing individual phases.

The assumption (2) that the 3D microstructure obtained by FIB-nt is representative of the original microstructure of undisturbed cement pastes sample can be questioned, as the sample preparation may affect the microstructure.

The sample preparation procedure includes freeze drying and subsequent epoxy impregnation [2]. Damage to the pore structure of cement paste caused by capillary forces developing during drying is reduced by freeze-drying compared to oven-drying [12]. Recently, a FIB-nt artefact study on the pore structure of hydrous bentonite was performed by comparing different types of drying and cryo-preparation techniques, in which the water in the samples was vitrified [13]. Significant artefacts caused by conventional drying were documented for bentonite samples with high water content (80 vol.%) only, while samples with lower water content showed almost no differences between different preparation techniques [13].

In the present investigation, FIB-nt volumes of freeze-dried and epoxy-impregnated 28-days old cement paste have been used (a single slice is shown in Fig. 1, left). Ordinary Portland cement was used; the water to cement ratio (w/c) of the paste was 0.3 while the curing temperature was 20 °C. From visual inspection, no drying artefacts can be suspected. Rather, magnified portions from the same sample show series of intact crystals which would likely have been damaged if significant drying artefacts had occurred (see clip of 5×5 μm^2 in Fig. 1, right).

Any suspicion of possible surface polishing artefacts can be likewise allayed, since each image area is sliced by means of ion beam milling. Typical damage that may occur is in the form of so-called waterfall artefacts exhibiting a vertical orientation [14]. Such grooves are thus easily discernible from the original structures and could not be observed in the samples examined in this paper.

Another source of uncertainty is the segmentation of the gray level image values to the pore mask. Indeed, the volumetric proportions of the phases can be significantly altered when modifying the segmentation threshold. Yet, some sophisticated filtering (discussed in Section 2.2) helps to lower the sensitivity to threshold values. Hence, a valid correlation of the original cement paste microstructure with the structures measured with FIB-nt can be achieved.

2.1. Methods

FIB-nt volumes ranging from 2600 to 7500 μm^3 with voxel size of 20 nm in all dimensions (Fig. 2, left) have been segmented into pores (P), hydration products (H) and unhydrated cement (U) (Fig. 2, right). The initial stacks of gray value images have first been aligned by detecting the maximum correlations. Subsequent noise reduction was performed with a novel 3D anisotropic diffusion filtering approach [15], using a non-linear and space-variant image transformation based on a generalized diffusion partial differential equation. The filter causes the blurred distributions of the original image values rearrange into distinct clusters (see Fig. 3), yielding clear peaks for porosity, hydration products, and clinker. After application of the filter, segmentation of the phases is therefore performed directly by thresholding (see Fig. 1, centre, and Fig. 2, right). For details of this procedure, the reader is referred to [11].

Uniformly distributed interaction volumes of size v have then been probed for their phase distribution p. The shape of the interaction volumes was set to cubes for simplicity reasons. In order to achieve smooth histograms, a large number of virtual interaction volumes (~100,000) have been probed. According to the typical size (~14^3 μm^3) of the FIB-nt volumes considered, this may lead to overlapping interaction volumes in case of $v > 300^3$ nm^3.

2.2. Results and discussion

The phase structure was scanned for the presence of distinct peaks in the porosity–hydration products-unhydrated cement (PHU) phase diagram, varying the size of the interaction volume v. Fig. 4 (left) shows a typical distribution of phase compositions

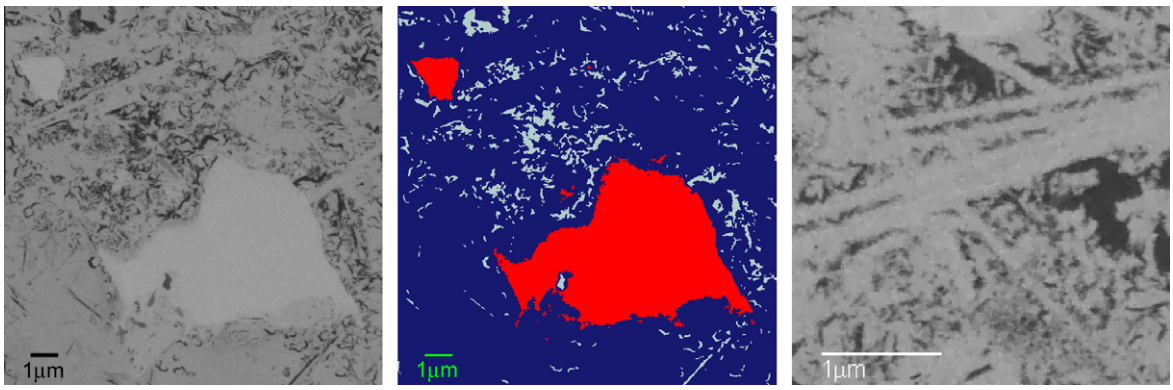

Fig. 1. Single slice from high-resolution 3D data volume of 28 days-old cement paste (CEM I, *w*/*c* 0.3) acquired with FIB-nt (left). Pores (gray), hydration products (blue) and unhydrated cement (red) can be segmented (centre). Magnified portions of FIB-nt images (5 μm × 5 μm) show well-preserved crystalline structures (right). (For interpretation of the references to colour in this figure legend, the reader is referred to the web version of this article.)

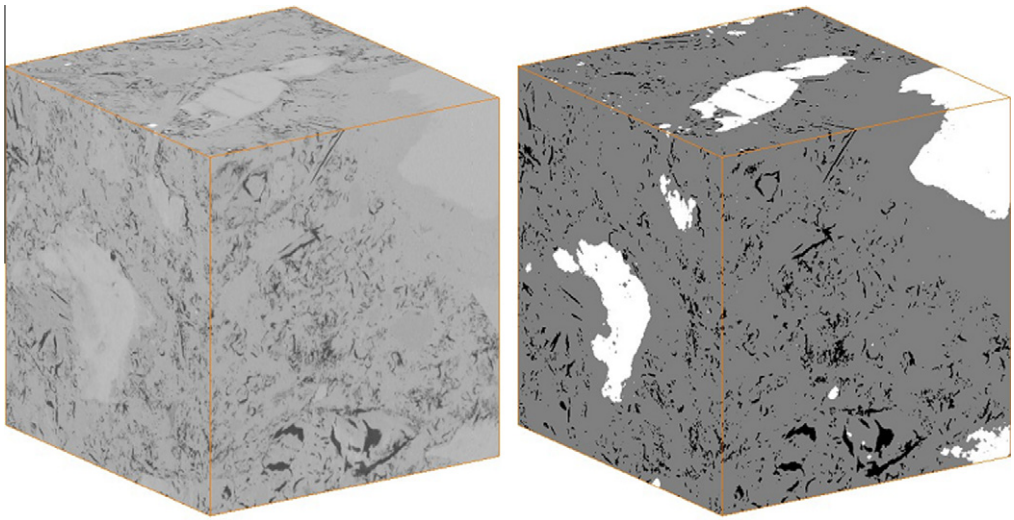

Fig. 2. Example of original (left) and segmented (right) FIB-nt volume (14.0 × 14.2 × 13.1 μm^3) with voxel size of 20 nm of a 28 days-old cement paste (CEM I, *w*/*c* 0.3). The dataset was filtered with an anisotropic diffusion filter followed by segmentation by simple thresholding. In the segmented volume (right), the pores (P) appear black, the hydration products (H) appear gray and the unhydrated cement (U) appears white.

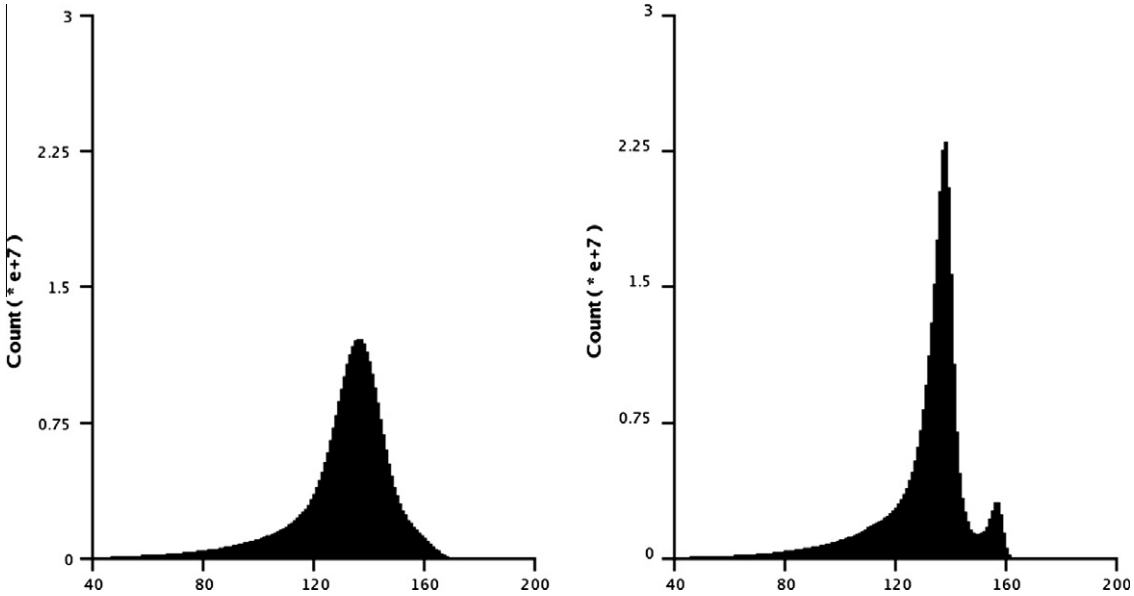

Fig. 3. Grayscale histogram of the original cement paste volume (left) and of the volume filtered with an anisotropic diffusion filter (right). Notice the separation of the originally single material peak into two phases which can be identified as hydrated products and unhydrated cement.

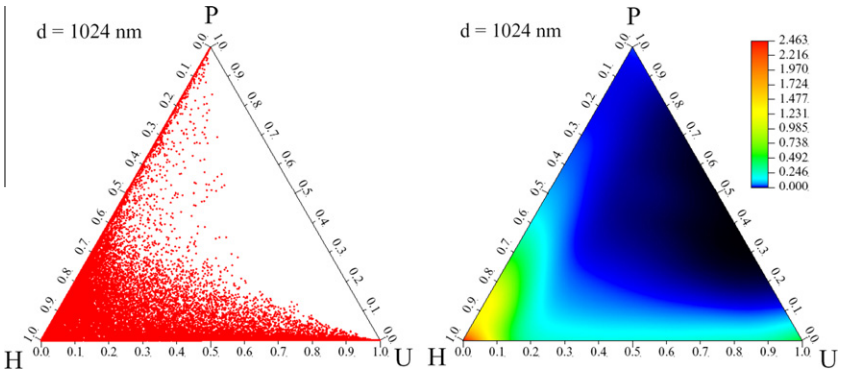

Fig. 4. Ternary plot of phase distributions in the probed interaction volumes of a FIB-nt sample ($14.0 \times 14.2 \times 13.1\ \mu m^3$) of cement paste with a size interaction volume of about 1 μm^3. The left figure shows the pores (P), hydration products (H) and unhydrated cement (U) phases for all locations; the right figure shows the same data in number of points per delta volume (Gaussian filtered density).

of a set of interaction volumes at $v = 1024^3\ nm^3$. The graph shows a clear clustering around the hydration phases (H). Since the total amount of porosity (P) is merely around 6.8%, and the amount of non-hydrated clinker (U) about 13.8%, none of these two phases shows a visible accumulation. The graph however shows that a considerable amount of phase composites is located close to one of the coordinate axes, pointing at dual-phase mixtures.

Since there are only few points in the inner part of the triangle showing triple-phase composites, whereas the local maxima are barely visible, an alternative way to present the results by showing the blurred and colour-coded densities of phase composites is provided. Fig. 4 (right) shows the same data as Fig. 4 (left) in this different representation. The 2D histogram was considerably blurred by using a Gaussian filter with a large sigma $\sigma = s/20$ (where s is the size of each coordinate axis). Such extensive blurring may of course wipe out possible local peaks, but on the other hand, it helps to emphasize global peaks. In order to make these peaks visible at high and at low image values, a highly non-linear colour coding was used (see lookup-tables in Fig. 4, right). This was especially necessary to favour eventual peaks at the less represented pore and non-hydrated clinker phases.

The ternary plots of the Gaussian-filtered phase distribution densities for varying sizes of the interaction volumes are shown in Fig. 5. Surprisingly, no peak corresponding to the actual phases present in the sample appear for $v > 1000^3\ nm^3$. Peaks at the three corners start to get established only at $v \leqslant 500^3\ nm^3$ and become clearly visible at $v \leqslant 250^3\ nm^3$. This means that phase clusters around the known phases are not recognizable on data of well-known phase geometry for interaction volumes v larger than about $500^3\ nm^3$. This finding relies on the pure material structure only, as it can be derived from high-resolution electron microscopy. Notice that the nanoindentation experiments themselves will introduce a

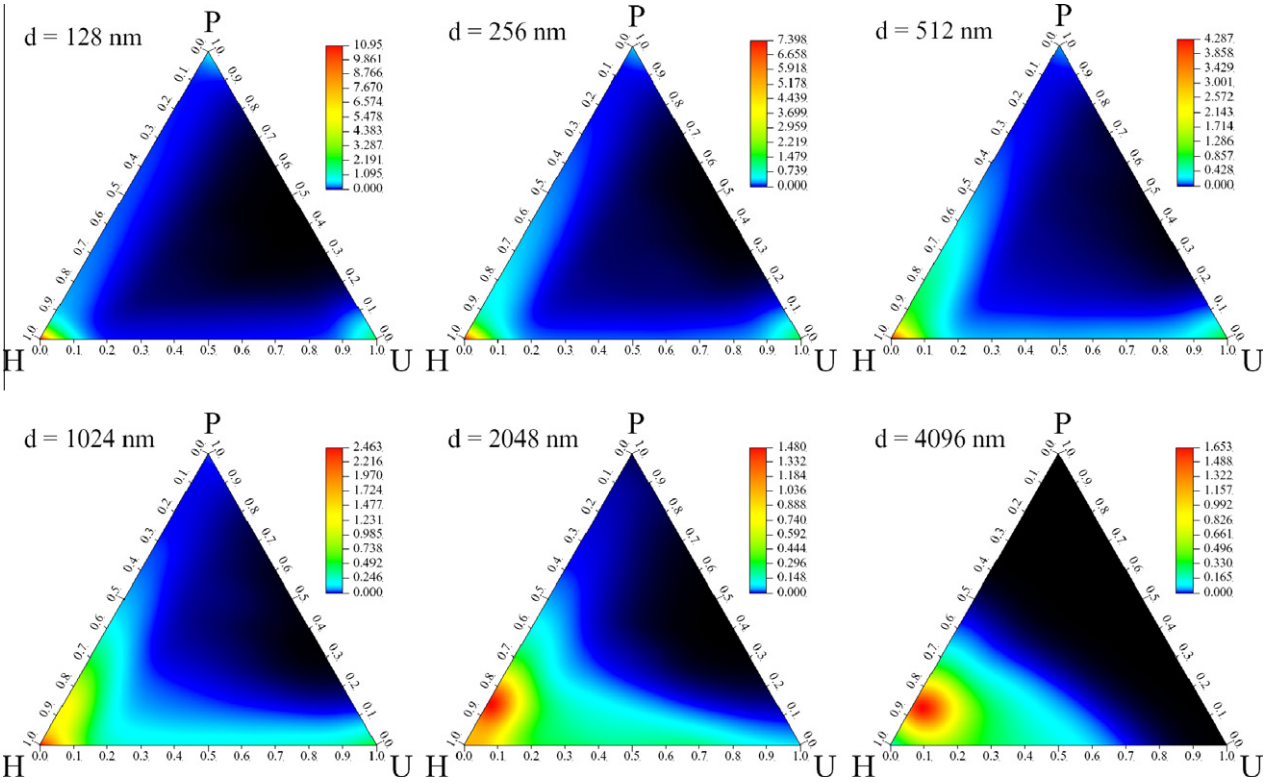

Fig. 5. Ternary plot of Gaussian-filtered phase distribution densities in the probed interaction volumes of a FIB-nt sample ($14.0 \times 14.2 \times 13.1\ \mu m^3$) at varying interaction diameters d.

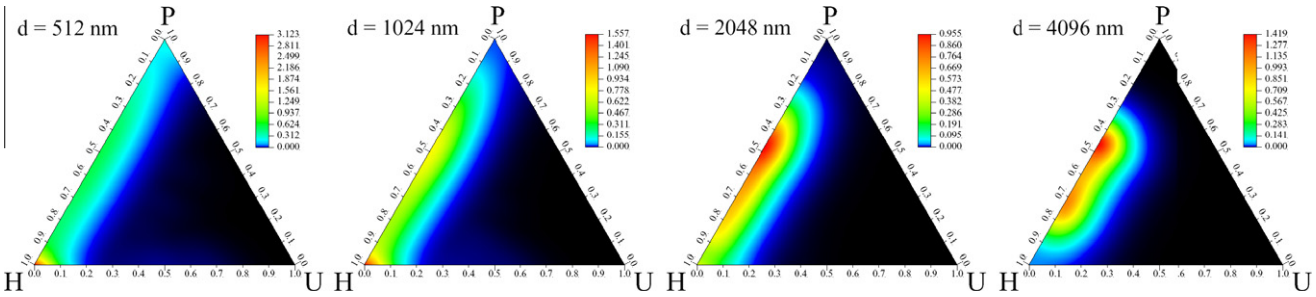

Fig. 6. Ternary plot of Gaussian-filtered phase distribution densities in the probed interaction volumes of a FIB-nt sample ($35.2 \times 26.5 \times 8.0\ \mu m^3$) of cement paste at varying interaction diameters d.

further scatter, which will be superimposed on the effect of the inhomogenous microstructure. Results of a second FIB-nt dataset are shown in Fig. 6. The other two datasets are not shown in this paper for the sake of brevity, but it is remarked that all four examined data volumes show a consistent pattern.

In some cases, the phase distributions may start to form peaks anywhere in the ternary plots at larger v (see Fig. 6), some of them already at $v = 1000^3\ nm^3$ which is the typical size of interaction volumes being responsible for the determination of the elastic moduli of the different phases [1,4,5]. According to Fig. 6, major peaks may appear at arbitrary phase compositions for interaction volumes larger than about $1\ \mu m^3$. This result implies that statistical nanoindentation may not be applicable to cement paste, when the nanoindentation interaction volumes are $1\ \mu m^3$ and larger.

3. Numerical instability of curve fitting

As the term "statistical nanoindentation" implies, the key to the determination of phase properties in the grid-indentation technique is the identification of the statistical distribution of the elastic modulus of the phases. It is noticed that whereas in the following only the distribution of the elastic moduli is addressed, our reasoning is more general and can also be extended to hardness distributions and to coupled distributions of hardness and elastic modulus [16]. The identification of peaks supposedly belonging to single phases is achieved by means of deconvolution of the elastic moduli density functions into sets of Gaussian functions [16].

Assuming a set of Gaussians $g_i(x) = f \cdot e^{-\left(\frac{x-\mu_i}{h_i}\right)\ln(2)}$, each $g_i(x)$ represents the distribution of a single phase and provides three free parameters, e.g. the mean value μ, the half width h and the height f amounting to the fraction of its specific phase. In case of three Gaussians (low and high density C–S–H, unhydrated clinker), this results in a 9-dimensional space where the optimum is expected to be found by mean squares error minimization (Eq. (3) in [16]). This essentially means finding the global optimum of a strongly non-linear function based on a set of numerical values in an n-dimensional space. Neither [16] nor any other reference about statistical nanoindentation gives any quantitative information about the algorithm for the optimum search. According to Vandamme et al. [16], in previous publications about statistical nanoindentation (e.g. [4]) the relevant optima have been found manually.

Typically however, such functions may produce a large number of local optima. Due to the high dimensionality of the parameter space, it is possible that an optimization process may converge to any one of those local optima. If so, then different results may be obtained by selecting different starting conditions.

3.1. Exploration of a characteristic example

Fig. 7 shows a recently published deconvolution (see Fig. 1 in [3]) of statistical nanoindentation data into four Gaussians denoting (from lowest to highest elastic modulus) low, high and ultra-high density (or LD, HD and UHD) C–S–H, and clinker. The original data was carefully extracted from the figure, whereas small errors cannot be completely excluded (compare the reproduced Fig. 7 with the original Fig. 1 in [3]). The reconstructed fit of four Gaussians corresponding to the values chosen by Ulm et al. [3] (see specifications in Table 1) achieves a $r^2 = 1 - s_\rho/s_o$ (s_ρ: variation of residuals, s_o: variation of original values) of 0.9239. Notice that no r^2 was declared in the original paper [3] and the former value has been reconstructed on the basis of the data extracted from Fig. 1 in [3]. The parameters for the Gaussians utilized in the fit of Fig. 7 are reported in Table 1.

In addition to possible imprecision, it is important to clarify some inevitable aberration of the extracted data relative to the original data:

(a) it is not completely clear whether the presented values stem from single indentation measurements, or whether some binning was already provided before;
(b) in addition to indentation modulus, the indentation hardness was provided in the original data [3]. However, it was not possible to consider the hardness data due to the unknown assignment (i.e., which hardness value belongs to which modulus value). The expected consequences are discussed in Section 3.3.

In order to provide an estimation about the instability of curve fitting on such kind of data, an optimization procedure has been established. Due to the highly non-linear characteristic of the least squares objective function (i.e., Eq. (3) in [16]), a downhill simplex algorithm achieving a tracking with an N-polytope (N: number of free dimensions) has been used [17]. In our example data aiming

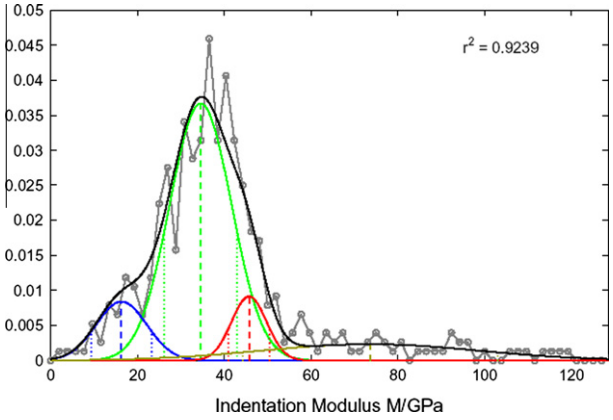

Fig. 7. Reproduction of statistical nanoindentation results (binned histogram of indentation moduli) as published in [3]. The r^2 of the fit relative to the binned data amounts to 0.9239 (see Table 1).

Table 1
Parameters for the Gaussians utilized in the fit of Fig. 7.

μ_1	μ_2	μ_3	μ_4	h_1	h_2	h_3	h_4	f_1	f_2	f_3	f_4	r^2
34.55	16.31	45.71	73.59	8.38	6.89	4.74	29.40	0.03673	0.008389	0.009123	0.002322	0.9239

at the optimization of four Gaussians, this simplex is a 12-polytope. The outstanding advantage of the used algorithm [17] is the flexible size of the N-polytope which is continuously being adjusted according to the local curvature of the objective function. The algorithm is fast and finds a single optimum within ~1.5 s on an Intel XEON 5430. The optimization was repeatedly applied on various initial simplices which have been randomly determined. Thereby, thousands of local optima could be found. In order to enforce some "realistic" Gaussian phase distributions, the following constraints have been required:

(a) all the Gaussian functions must be positive;
(b) the Gaussian mean values are constricted to 0 GPa < μ_j < 130 GPa, corresponding to the expected interval of the moduli of the single phases;
(c) each new optimum has been checked against any previously found optimum, to verify whether the new optimum was differing at least by 10% in at least one of the 12 dimensions.

Any optimum outside of the above constraints was rejected.

Beyond, the optimization procedure was extended in order to enforce equivalent half widths h_i for the Gaussians. This modification is interesting because it is remarkable that the clinker phases show much wider Gaussians compared to the narrower C–S–H phase distribution in the discussed diagram [3] as well as in other deconvolved results from statistical nanoindentation [5,16]. In fact, clinker has low porosity and is composed of phases which have similar elastic modulus [18]; on the contrary, hydration products are composed of multiple phases of very different moduli and have large and inhomogenous porosity. In addition, due to the high modulus and hardness of clinker, the interaction volume should be smaller than in the case of hydration products [3]. According to these considerations, one would expect to obtain narrower Gaussians for the clinker and broader for the hydration products, while the opposite is the case [3,5,16]. In addition, the average values of elastic moduli of clinker found by statistical nanoindentation on cement paste [3,5,16] are much lower than the values found by indenting the clinker [18].

3.2. Results

A total of 30,000 varying local optima have been identified. About 98.6% of all local optima provided fits with r^2 above 0.9239, which is the estimated r^2 of the fit shown in Fig. 7 [3]. The limitation according to constraint (c) resulted in 68% of the optima being rejected, yielding a total of 9788 remaining optima. The highest r^2 found amounted to 0.9614.

A list of fits for the optimization of 4 Gaussians is provided in Fig. 8 and also in Table 2. The r^2 values range from 0.9504 to 0.9614 and are thus much better than the one provided in Fig. 7 [3]. It is important to note that there are many different ways of curve fitting for achieving excellent r^2, which however yield completely different distribution characteristics. None of the distributions shown in Fig. 8 resembles in the least the one in Fig. 7. We notice that the observation that many better fits are possible with totally different characteristics from the fit in Fig. 7 does not represent a definitive statement against this fit. However, this observation shows that the fit of Fig. 7 is based on a model postulating three types of C–S–H with distinct elastic moduli (LD, HD [19] and UHD C–S–H [3,5]), rather than being an independent proof for this model.

Further optimizations by either introducing constraints or by lowering the number of Gaussians are presented in Fig. 9 and also in Table 3. The first case (case 7 in Fig. 9) shows the Gaussians at the same μ_i as in Fig. 7 but optimized letting h_i and f_i vary, yielding an improved r^2 of 0.9328 instead of 0.9239. If in addition to μ_i the same half width for all Gaussians was required (which makes sense for simple statistical reasons), the achieved r^2 = 0.9289 would still be higher compared to the original fit in [3] (case 8 in Fig. 9).

The next two cases (9 and 10 in Fig. 9) show local optima at equivalent half width but arbitrary μ_i yielding r^2 = 0.9379 and 0.9414, the former case showing an optimum that might be preferable for substantiating Jennings model [19], the latter for yet another model to be created. Finally, the last two cases (11 and 12 in Fig. 9) show that fits superior to the original one could also be achieved by using only 3 (r^2 = 0.9430) or even only 2 (r^2 = 0.9314) Gaussians. Importantly, the last two cases show that fitting the results of the cement paste investigated in [3] with four Gaussians (i.e., three types of C–S–H and unhydrated clinker) is only one of the available possibilities. Our results show that the same statistical nanoindentation results can be fitted by a different number of Gaussian peaks (i.e., material phases), still obtaining similar or better r^2. As a consequence, the statistical nanoindentation datasets as presented in [3] could be also used for supporting the presence in the investigated hardened cement pastes of only one, or only two, C–S–H types.

3.3. Discussion

The large number of detected local optima might be surprising. Yet, one must keep in mind that in the case of 4 Gaussians we are optimizing in a 12-dimensional parameter space. This means that a regular grid with a total number of M Gaussian fits is located at $m \approx \sqrt[12]{M}$ points on each axis, i.e., slightly more than two points per dimension in the case of M = 9788 fits. This is indeed a very low number when considering the large scattering of the measured data. It can be expected that similar numbers of local optima could also be easily found on other nanoindentation datasets.

The most remarkable finding is not the number of optima, but the large variety of the basic characteristic of the optimum fits (Fig. 8).

Table 2
Parameters for the Gaussians utilized in the different fits (1–6) shown in Fig. 8. The fits were calculated with 4 Gaussian functions each and no constraints.

No. of fit	1	2	3	4	5	6
μ_1	26.07	17.23	35.37	26.07	20.14	25.03
μ_2	31.16	25.97	36.49	31.57	25.93	25.97
μ_3	34.18	37.37	40.90	38.21	37.62	37.55
μ_4	38.42	52.31	40.35	60.93	68.20	41.10
h_1	1.070	4.916	11.20	1.138	9.517	12.34
h_2	0.8498	0.4377	0.4006	15.16	1.505	1.372
h_3	20.13	8.337	1.419	6.982	8.500	8.170
h_4	6.108	41.68	54.29	42.16	27.02	41.71
f_1	0.02156	0.007382	0.02902	0.01352	0.008153	0.003038
f_2	0.01471	0.3314	0.01449	0.01251	0.005303	0.01149
f_3	0.01225	0.03636	0.01366	0.02625	0.03663	0.03268
f_4	0.02780	0.002961	0.002736	0.002177	0.002724	0.004212
r^2	0.9614	0.9589	0.9576	0.9557	0.9504	0.9504

Table 3
Parameters for the Gaussians utilized in the different fits (7–12) shown in Fig. 9. The fits were calculated fits with a variable number of Gaussian functions as well as variable constraints, as indicated in the table for each fit.

No.	7 4 Gaussians, same μ as Fig. 7	8 4 Gaussians, same μ as Fig. 7, equivalent h	9 4 Gaussians, equivalent h	10 4 Gaussians, equivalent h	11 3 Gaussians, no constraint	12 2 Gaussians, no constraint
μ_1	34.55	34.55	38.87	37.58	32.77	36.37
μ_2	16.31	16.31	15.06	20.31	39.38	31.16
μ_3	45.71	45.71	27.49	92.07	51.89	–
μ_4	73.59	73.59	65.30	65.81	–	–
h_1	8.729	8.639	8.257	9.106	11.93	9.810
h_2	6.412	8.639	8.257	9.106	6.130	50.31
h_3	7.0252	8.639	8.257	9.106	43.63	–
h_4	28.24	8.639	8.257	9.106	–	–
f_1	0.03428	0.03291	0.03437	0.03737	0.02098	0.03377
f_2	0.006628	0.006107	0.004354	0.008443	0.01847	0.003685
f_3	0.009613	0.01103	0.01176	0.002138	0.002809	–
f_4	0.002273	0.003044	0.003682	0.003315	–	–
r^2	0.9328	0.9289	0.9379	0.9414	0.9430	0.9315

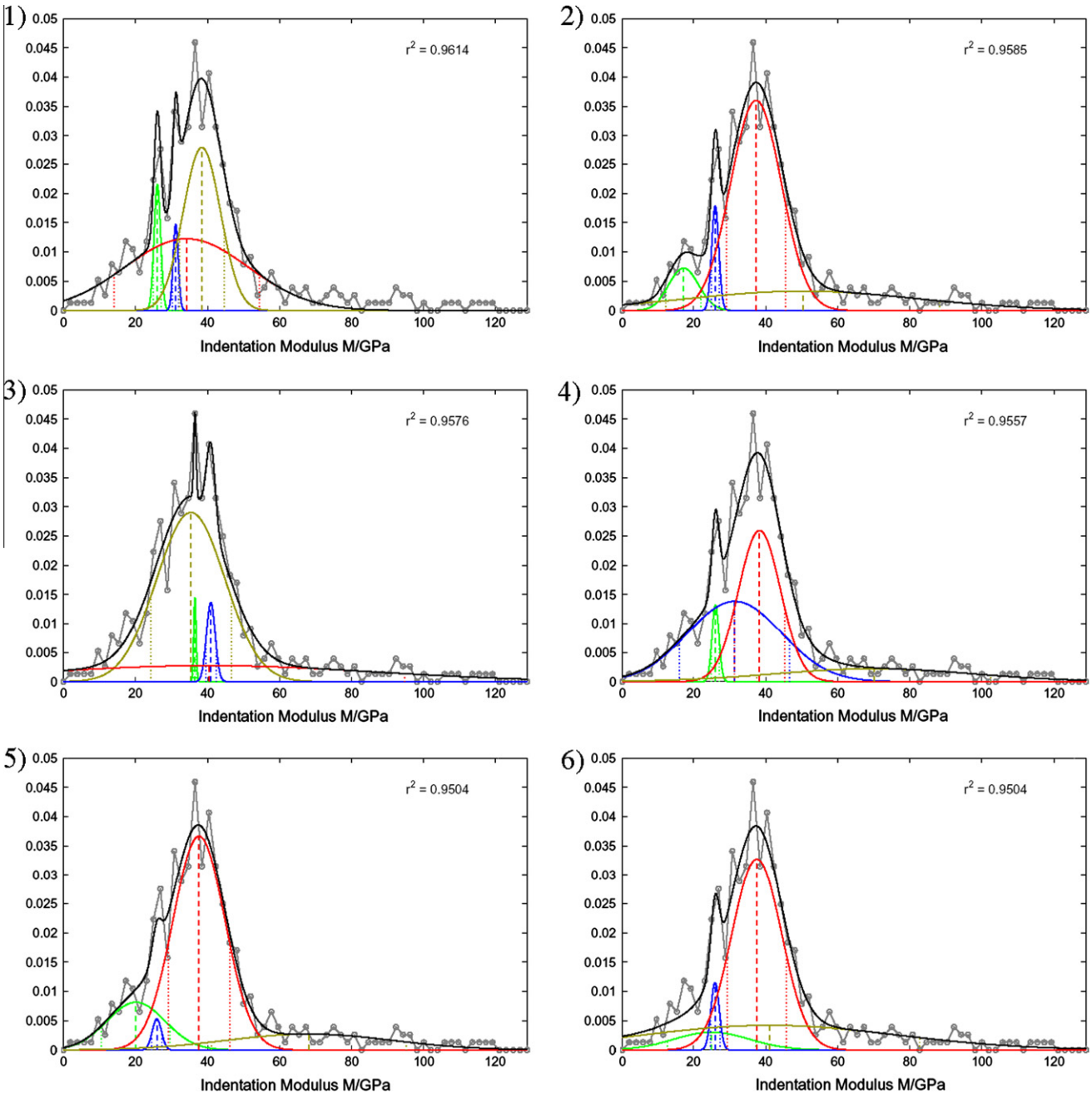

Fig. 8. Same data as presented in Fig. 7, fitted by alternative Gaussian fits resulting in better r^2 (see Table 2).

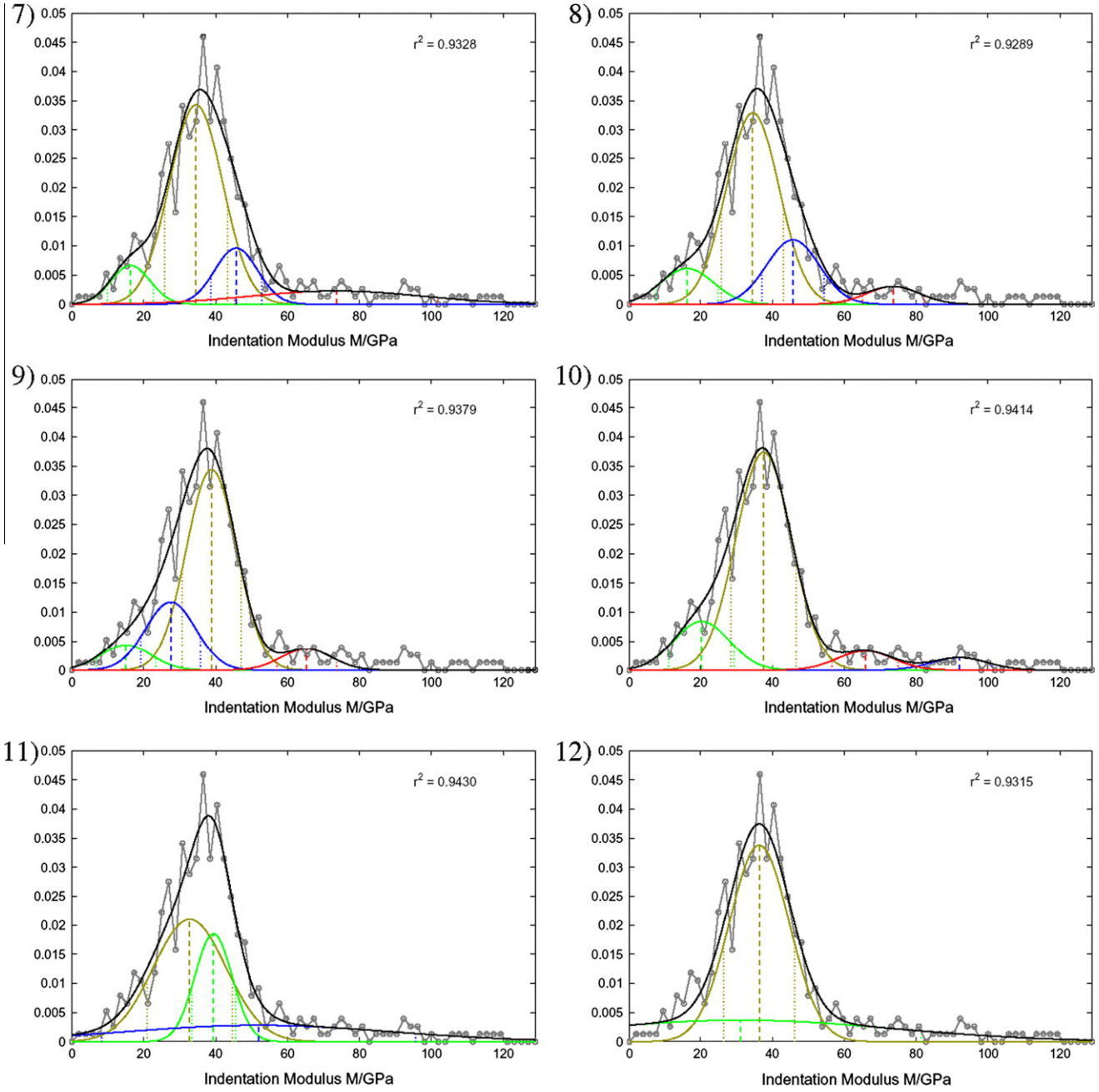

Fig. 9. Same data as presented in Fig. 7, fitted by alternative Gaussian fits resulting in better r^2 (see Table 3).

Perhaps, one might claim that simultaneously optimizing two indentation quantities, indentation modulus and hardness, will improve the robustness of the optimization procedure [16]. This claim looks persuasive, as any two connected modulus and hardness values are supposed to be classified into the compliant classes. However, strongly depending on the measured data, this does not necessarily imply a lower number of local optima. On the contrary, even the opposite could be true. In fact, fitting the second dataset comes along with a tremendous increase of the dimensionality of the optimized parameter space, since each class will now be connected to two instead of one Gaussians only, i.e., one for the moduli and one for the hardness values. Depending of how conformably the set of measured tuples can be associated to coinciding phase classes, a second set of values may either reinforce the robustness of the optimization or even produce an increase of the error rate, if some of the class memberships are not coinciding. Regarding the dataset presented in Section 3.2, this might even be one of the reasons for the substantially lower r^2 values achieved according to the fit presented by Ulm et al. [3] (Fig. 7), compared to the fits calculated in this paper (Figs. 8 and 9).

One might also claim that according to [16], the optimization should not be performed on the binned original data of the measured indentation moduli, but rather on their cumulative distribution function. Nanoindentation data are evaluated in such a way in order to be independent from any pre-selected size of histogram bins [16]. Such argumentation itself gives an impression about the presumably large scatter in the original histogram data – which is actually noise produced by working with small datasets. The only convincing remedy would be a considerable increase of the number of data points, which would supersede the need for forming bins. The

recommended integration indeed helps to diminish the signal noise; however, this has no effect to the number of local optima.

Referring to the data that was retrieved from the plots, it must be noted that by taking any dedicated binning, the complexity of the optimization function (Eq. (3) in [16]) becomes simplified, since binning means low-pass filtering of the original histogram. Low-pass filtering clearly involves a reduction of the total number of local optima. Consequently, the number of local optima from the original data can be expected to be even larger than the number of optima from its binned representation. The best and fastest of all existing algorithms will never be able to detect the global optimum reliably for a set of statistical nanoindentation data. But even if the algorithm used in this paper was probably not the best of all choices, the long list of detected local optima shows that there is a vast number of alternative fits.

4. Conclusions

In this paper, we examined different aspects of the statistical nanoindentation technique, in particular the influence of the microstructure on the statistical nanoindentation results (Section 2) and the procedure for fitting the statistical nanoindentation plots (Section 3).

The results of the virtual experiment presented in Section 2 face us with only two possible conclusions: either, the microstructure in cement paste is very different from the structures revealed by FIB-nt or SEM in general, or statistical nanoindentation experiments on cement paste with interactions volumes of 1 μm^3 and larger, used to determine single-phase elastic moduli and hardness, are invalid.

The large variety of possible Gaussian fits (Section 3) indicates that statistical nanoindentation data of the quality that is currently being published cannot be used to prove any model about C–S–H, such as the one proposed by Jennings [19]. Our results show that the published deconvolution of the nanoindentation data is itself based on model assumptions about bimodality or trimodality [3] of elastic moduli of C–S–H. This evidence does not disqualify Jennings model [19] or the idea of statistical nanoindentation as such, but it cautions against using statistical nanoindentation according to the current state-of-the-art of the technique for validating structural models on complex materials.

Acknowledgements

The authors thank Dale Bentz, Ed Garboczi and Andreas Leemann for critical reading of the manuscript and useful discussion.

References

[1] Constantinides G, Ulm FJ. The effect of two types of C–S–H on the elasticity of cement-based materials: test results from nanoindentation and micromechanical modeling. Cem Concr Res 2004;34:67–70.
[2] Trtik P, Münch B, Lura P. A critical examination of statistical nanoindentation on model materials and hardened cement pastes based on virtual experiments. Cem Concr Compos 2009;31:705–14.
[3] Ulm F-J, Vandamme M, Jennings HM, Vanzo J, Bentivegna M, Krakowiak KJ, et al. Does microstructure matter for statistical nanoindentation techniques? Cem Concr Compos 2010;32:92–9.
[4] Constantinides G, Ulm FJ. The nanogranular nature of C–S–H. J Mech Phys Solids 2007;55:64.
[5] Chen JJ, Sorelli L, Vandamme M, Ulm F-J, Chanvillard G. A coupled nanoindentation/SEM–EDS study on lowwater/cement ratio portland cement paste: evidence for C–S–H/$Ca(OH)_2$ nanocomposites. J Am Ceram Soc 2010;93:1484–93.
[6] Hughes JJ, Trtik P. Micro-mechanical properties of cement paste measured by depth-sensing nanoindentation: a preliminary correlation of physical properties with phase type. Mater Charact 2004;53:223–31.
[7] Trtik P. Focused Ion Beams (FIB) – tools for serial sectioning of nanoindentation sites in cementitious materials. In: Bartos, Hughes, Trtik, Zhu, editors. 'Nanotechnology in construction'. Proc. 1st symp. on nanotechnology in construction (NICOM 1). Royal Society of Chemistry: Paisley, Scotland, UK; 2003. p. 53–61 [ISBN 0-85404-623-2].
[8] Trtik P, Reeves CM, Bartos PJM. Use of focused ion beam (FIB) for advanced interpretation of microindentation test results applied to cementitious composites. Mater Struct 2000;33:189.
[9] Holzer L, Indutnyi F, Gasser P, Münch B, Wegmann M. Three-Dimensional Analysis of Porous $BaTiO_3$ Ceramics Using FIB Nanotomography. J Microsc (Oxf) 2004;216(1):84–95.
[10] Trtik P, Dual J, Muench B, Holzer L. Limitation in obtainable surface roughness of hardened cement paste: 'virtual' topographic experiment based on focussed ion beam nanotomography datasets. J Microsc (Oxf) 2008;232:200.
[11] Trtik P, Münch B, Gasser P, Leemann A, Loser R, Wepf R, Lura P. Focussed ion beam nanotomography reveals the 3D morphology of different solid phases in hardened cement pastes. J. Microsc. (Oxf); 2011. doi: 10.1111/j.1365-2818.2010.03433.x.
[12] Ye G. Experimental study and numerical simulation of the development of the microstructure and permeability of cementitious materials. PhD thesis. Delft University of Technology; 2003.
[13] Holzer L, Münch B, Rizzi M, Wepf R, Marschall P, Graule T. 3D-microstructure analysis of hydrated bentonite with cryo-stabilized pore water. Appl Clay Sci 2010;47:330.
[14] Münch B, Trtik P, Marone F, Stampanoni M. Stripe and ring artifact removal with combined wavelet – Fourier filtering. Opt Express 2009;17:8567.
[15] Tschmperlé D, Deriche R. Vector-valued image regularization with PDE's: a common framework for different applications. IEEE Trans Pat Anal Mach Intell 2005;27:506.
[16] Vandamme M, Ulm FJ, Fonollosa P. Nanogranular packing of C–S–H at substochiometric conditions. Cem Concr Res 2010;40:14.
[17] Nelder JA, Mead R. A simplex method for function minimization. Comput J 1965;7:308.
[18] Velez K, Maximilien S, Damidot D, Fantozzi G, Sorrentino F. Determination by nanoindentation of elastic modulus and hardness of pure constituents of Portland cement clinker. Cem Concr Res 2001;31:555–61.
[19] Jennings HM. A model for the microstructure of calcium silicate hydrate in cement paste. Cem Concr Res 2000;30:101.